大阪工業大学紀要 (2026)　投稿原稿

Gravitational-wave Extraction using Independent Component Analysis

Rika Shimomura, Yuuichi Tabe, Hisaaki Shinkai

Faculty of Information Science and Technology

(2026 年　月　日受理)

Abstract

Independent component analysis (ICA) is a method of extracting a set of time-series data based on the statistical independence of each component. We applied ICA to extract gravitational wave (GW) signals directly from the detector data. The idea is to extract a coherent signal that is included in multiple detectors and find it by shifting the data set around its arrival time. In this article, we present the results of several tests involving injected signals, and demonstrate that this method is effective for inspiral-wave events with a signal-to-noise ratio (SNR) of greater than 15. We then applied the method to actual LIGO-Virgo-KAGRA O1-O3 events (high-SNR binary black hole events), and demonstrated that the arrival time could be identified more precisely than had been reported previously. This approach does not require waveform templates, making it attractive for testing theories of gravity, and for detecting unknown GWs.

Keyword; Gravitational Wave, Data Analysis, Independent component analysis

1 Introduction

A decade has passed since the LIGO-Virgo collaboration made the first detection of a gravitational wave (GW), known as GW150914 [1]. The LIGO-Virgo-KAGRA (LVK) collaboration has reported 90 GW events in the GWTC-3 catalogue, which is the result of the O3 observing run which ended in March 2020 [3]. The catalogue comprises 90 events from compact binary coalescence (CBC), 85 of which are from binary black holes (BHs). The LVK collaboration plans to announce the next catalogue in the coming months, in which we expect the number of detections to double [1]. In short, we are entering an era of GW astronomy.

As the number of events increases, various aspects of astronomy and physics can be explored. For example, it is unclear how super-massive BHs are formed in the center of galaxies. This problem requires an understanding of BH formation processes, including its formation and merger rates, which can be explained by the statistics of GW detections (see the references in [4, 5]). We are unsure how general relativity (GR) is consistent with quantum theory. This viewpoint requires the validity of GR, which can be best tested in strong-gravity regimes, such as the merger of BHs (see the references in [6, 7]).

GW signals are very weak and are often obscured by the noisy outputs of detectors. The main method of detecting GWs from CBCs is analysis based on matched-filtering. This method uses a template bank of waveforms and which measures the correlation between a template and the observed signal. The LVK collaboration currently uses their detection pipelines based on this "modeled search", named LALInference [8], GstLAL[9], MBTA[10], PyCBC [11], Bilby[12] and SPIIR[13]. However, this method is based on a prepared set of templates and is ineffective for others. LVK also uses their pipelines with an "unmodeled search", such as cWB[14], oLIB [15], and MLy[16]. This method searches for coherent excess power signals in multiple detectors and produces a time-frequency diagram for the initial bet.

While there are various approaches as mentioned above, we would like to propose a new method that belongs to the latter category. Our aim is to obtain the waveform itself through "unmodelled search". If we could identify GW signals without using prepared templates, then we could test gravity theories (including GR) systematically. We could also feed back into modeling supernova explosions, stochastic events etc, and also it would be possible to discover previously unknown types of gravitational wave. Several new ideas have been proposed in this regard. One idea is to process time series data using mathematical and/or statistical techniques. Another idea is to use machine learning approaches (see the comparison of these techniques for extracting ringdown mock data [7] and the references therein).

In this article, we introduce independent component analysis (ICA) as a method of extracting GW signals directly from detector output data. ICA is a method of separating a set of time series data into new components, each of which has "statistical independence" (see the review by Hyvärinen *et al.* [17, 18]). A well-known example is "blind signal separation," a method used to identify the voices of n people at a cocktail party from mixed sound files recorded by n microphones. See [19] for the case of $n = 10$. ICA provides a linear representation of non-Gaussian data, ensuring that the components are statistically independent or as close to it as possible. The fundamental measure is the degree of separation from the Gaussianity. Therefore, in GW data analysis, we can expect that GW extraction using ICA to be effective, at least when the background noise is Gaussian.

We highlight the differences between ICA and principal component analysis (PCA) of which applications to GW analysis have been reported recently [20, 21, 22, 23]. Both aim to extract data in a lower-dimensional space from the original data, but their criteria differ. PCA is based on the principle of uncorrelation, which maximizes the variance of the data. ICA, on the other hand, is based on statistical independence; in other words, no information can be obtained from other components. This is a stronger requirement than uncorrelation. PCA is suitable for dimensional reduction capturing the main direction of large variance, data visualization and noise removal, whereas ICA is effective for separating mixed signals and extracting hidden independent components.

The use of ICA for GW data analysis was first reported by De Rosa *et al.* [24]. They demonstrated ICA for injected signals in mimicking two interferometer data and reported that preprocessing ICA before applying the matched filtering technique reduces the level of noise (thereby increasing the signal-to-noise ratio (SNR)). Morisaki *et al.* proposed the application of ICA to non-Gaussian noise subtraction [26]. Using

[1]While we are preparing this article, the LVK collaboration released their new catalogue, GWTC-4.0, which is the result of the first period of the O4 observing run (O4a) which ended in January 2024 [28, 29, 30]. This catalogue includes 86 new events, 84 of which are from binary BHs.

their idea, the KAGRA collaboration reported an application to their real data (iKAGRA data in 2016) to obtain an enhanced SNR using physical environmental channels (i.e. seismic channels) as known signals[25].

In this article, we present our attempts to extract GW signals directly using ICA. We demonstrate how injected data can be extracted from Gaussian noise or real detector output, and present our trials with actual GW event data. GW events are fundamentally identified using the coherence of multiple interferometers, taking into account the difference in arrival time (up to 10 ms between Livingston and Hanford and 30 ms between Hanford and Virgo). We have developed a tool for extracting real GW signals by shifting the multiple-detector dataset around its arrival time. Consequently, the arrival time differences between the detectors can be estimated more precisely than was previously reported.

The remain of this report is structured as follows. In Section 2, we explain the fundamental concept of ICA and our basic procedures. In Section 3, we present some tests using injected data for Gaussian noise and actual detector noise. In Section 4, we present the results of the extractions of GW from binary black-hole mergers in O1-O3. Our conclusions and outlook are presented in Section 5.

2 Independent Component Analysis

2.1 The fundamental procedures of ICA

Suppose we receive the time-series signal $\boldsymbol{x}(t) \equiv (x_1(t), \cdots, x_n(t))^T$ with n detectors from n source signals $\boldsymbol{s}(t) \equiv (s_1(t), \cdots, s_n(t))^T$, and they are mixed linearly by

$$\boldsymbol{x}(t) = A\boldsymbol{s}(t), \tag{1}$$

where A is a time-independent matrix that represents the superposition of source signals. ICA is a method for extracting a (candidate) signal $\tilde{\boldsymbol{s}}(t)$ from $\boldsymbol{x}(t)$.

We write the problem as

$$\tilde{\boldsymbol{s}}(t) = W\boldsymbol{x}(t), \tag{2}$$

and set the goal to find a time-independent matrix W, so as $\tilde{\boldsymbol{s}}(t)$ contains meaningful signal information. We, heareafter, call $\boldsymbol{x}(t)$ and $\tilde{\boldsymbol{s}}(t)$ input signals (to ICA) and output signals (from ICA), respectively.

In the GW case, we expect that a real GW signal is commonly included in all components of $\boldsymbol{x}(t)$. Our goal is to find a GW signal in a single component of the output signal $\tilde{\boldsymbol{s}}(t)$, whereas the other components are noise.

ICA uses the idea of "statistical independence" of each source signal component $\tilde{\boldsymbol{s}}$. Roughly speaking, "statistical independence" can be evaluated as how far from Gaussianity. (Hence, ICA is not appropriate for extracting Gaussian signals since their superposition is Gaussian.)

A standard method of ICA starts from whitening the input data, which we mean that $\boldsymbol{x}(t)$ is transformed to $\boldsymbol{z}(t)$ so as to have no-correlation and its variance unity, where we write

$$\boldsymbol{z}(t) = V\boldsymbol{x}(t). \tag{3}$$

We then write i-th component of $\tilde{\boldsymbol{s}}(t)$ as

$$s_i(t) = \boldsymbol{w}_i^T \boldsymbol{z}(t), \tag{4}$$

where $\boldsymbol{w}_i$ is i-th row of W. The objective is to find W as it gives $s_i(t)$ with (mostly) statistical independence.

One possible measure of non-Gaussianity is to use the kurtosis of $\boldsymbol{w}_i^T\boldsymbol{z}$, and a well-known algorithm (FastICA) was first developed using kurtosis to find $\boldsymbol{w}_i$ using an iterative method (see Appendix A for further explanation). However, this method is known to be sensitive to outliers. We also met this fact, and decided to use alternative FastICA known as the g-function method, which uses a mimic function to the kurtosis. The target procedure is to find $\boldsymbol{w}_i$ that satisfies

$$\boldsymbol{w}_i = E[\boldsymbol{z}g(\boldsymbol{w}_i^T\boldsymbol{z})] - E[g'(\boldsymbol{w}_i^T\boldsymbol{z})]\boldsymbol{w}_i \tag{5}$$

where $g(y) = \tanh y$.

Our procedure can be summarized as follows. Let p be the number of iterations.

1. Whiten the data $x(t)$ using the power spectral density of each detector and apply filtering if necessary.

2. Normalize $x(t)$ to $z(t)$ (mean zero, variance one). [eq. (3)]

3. Set index $i = 1$.

4. Randomly choose an initial weight matrix $\boldsymbol{w}_i^{(p)}$.

5. Obtain $\boldsymbol{w}_i^{(p+1)}$ from (5) as

$$\boldsymbol{w}_i^{(p+1)} = E[\boldsymbol{z}g(\boldsymbol{w}_i^{T(p)}\boldsymbol{z})] - E[g'(\boldsymbol{w}_i^{T(p)}\boldsymbol{z})]\boldsymbol{w}_i^{(p)}. \tag{6}$$

6. Orthogonalize $\boldsymbol{w}_i^{(p+1)}$ from the other components,

$$\tilde{\boldsymbol{w}}_i^{(p+1)} = \boldsymbol{w}_i^{(p+1)} - \sum_{j=1}^{i-1} (\boldsymbol{w}_i^{T(p+1)} \boldsymbol{w}_j) \boldsymbol{w}_j. \quad (7)$$

7. Normalize $\tilde{\boldsymbol{w}}_i^{(p+1)}$ as $\boldsymbol{w}_i^{(p+1)} = \tilde{\boldsymbol{w}}_i^{(p+1)} / \|\tilde{\boldsymbol{w}}_i^{(p+1)}\|$.

8. If $\boldsymbol{w}_i^{(p+1)}$ does not converge to the previous $\boldsymbol{w}_i^{(p)}$, then return to (v).

9. Set i to $i+1$. If i is smaller than the number of components of $\boldsymbol{x}$, then return to (iv).

To confirm that our converged $\boldsymbol{w}_i$ was unique, we repeated the procedure at least five times, changing the initial trial weight matrix $\boldsymbol{w}_i^{(p=0)}$ (procedure iv). As we will show later in Figure 5, the converged solution is obtained in most cases within 10-30 cycles of the iteration, while a different solution was rarely converged for the initial $\boldsymbol{w}_i^{(p=0)}$. We confirmed that the majority of the five $\boldsymbol{w}_i^{(p=0)}$ trials indicate realistic signal extraction for all cases, using the detection criterion $\mathcal{A}$, which is later defined as eq. (10).

Note that the output signals from the ICA do not have amplitude information because the data are normalized first. The phase of the output signals can be reversed due to the signature of $\det(W)$. Further studies are required to identify them. (See Section 5.)

The order of $\tilde{s}_1, \tilde{s}_2, \cdots$ represents the order of the independent signals founded by the code. We found that this order sometimes changes due to the initial $\boldsymbol{w}_i^{(p=0)}$. This order is independent of the amplitude of the input signal. We also found that the inspiral GW signal in the ICA output has the largest amplitude, regardless of the order, $\tilde{s}_1, \tilde{s}_2, \cdots$. While we believe it is unnecessary to consider the order, to avoid confusion, we will present figures showing GW signals are in $\tilde{s}_1$.

2.2 Measure for identification of GW

For the injection tests (Sec. 3), we evaluated the output signal by comparing it with the injected signal, using its waveform and spectrum. When we test with an injection of an inspiral-wave signal, the waveform $h_{\rm insp}$ is

$$h_{\rm insp}(t; t_c, M_c) = A_{\rm insp} \left(\frac{5}{c(t_c - t)} \right)^{1/4} \times \sin \left\{ -2 \left(\frac{5GM_c}{c^3} \right)^{-5/8} (t_c - t)^{5/8} \right\}, \quad (8)$$

where c, G, M_c, t_c are the speed of light, gravitational constant, chirp mass, and merger time, respectively. The factor of the amplitude $A_{\rm insp}$ can be written as $A_{\rm insp} = (1/r) \left(GM_c/c^2 \right)^{5/4}$, where r is the distance to the source. As we analyze later, we work in the detector frame and use $A_{\rm insp}$ as a parameter, instead of the distance, r.

For the real GW extraction (Sec. IV), we compared the components of the output signals $\tilde{s}_i(t)$, by defining the "signal strength" $\mathcal{A}$ [Eq. (10)] using the area of the signal in the graph

$$A_i = \sum_{t=t_s}^{t_c} \tilde{s}_i(t) \cdot \Delta t, \quad (9)$$

where t_c is the time of coalescence and $t_s = t_c - 15$ ms for binary black-hole data.

Let $\tilde{s}_1(t)$ be the candidate of the GW signal and the others ($\tilde{s}_2(t)$ for two detector events; $\tilde{s}_2(t)$ and $\tilde{s}_3(t)$ for three detector events) be detector noises. We evaluate the ratio

$$\mathcal{A} = \begin{cases} \dfrac{A_1}{A_2} & \text{for 2 detector event} \\ \dfrac{2A_1}{A_2 + A_3} & \text{for 3 detector event,} \end{cases} \quad (10)$$

as "signal strength" to the other remained signals. A larger $\mathcal{A}$ suggests that $\tilde{s}_1(t)$ has a larger amplitude than the others.

We also compare the candidate signal $\tilde{s}_1(t)$ and the estimated inspiral waveform using the chirp mass M_c reported in GWOSC (Gravitational Wave Open Science Center) website [27], $h_{\rm insp}(t; t_c, M_c)$, by taking the residuals

$$\mathcal{R} = \sum_{t=t_s}^{t_c} |\tilde{s}_1(t) - h_{\rm insp}(t; t_c, M_c)| \cdot \quad (11)$$

Smaller $\mathcal{R}$ suggests better extraction than the others.

2.3 Finding the arrival time

One of the key procedures of our proposal involves determining the arrival time of the GW signal at each detector by continually shifting the input data. While such an implementation is not necessary for normal applications of the ICA method, it is necessary for GW signals.

In this article, we only demonstrate the applications for known events up to O3, therefore, the merger time, t_c, is taken as a given suggested value. We then search for the GW signal around t_c by shifting the data from each detector by up to ± 30 ms (the approximate distance between Hanford and Virgo), and search for the combination that shows the largest $\mathcal{A}$. As we show in Table 3, the result of the shifted time, for example, $\Delta t_{\mathrm{HL}}(=t_{\mathrm{L}}-t_{\mathrm{H}})$ between Hanford and Livingston, can be identified as the difference in GW arrival times, and its comparison with those in published articles will also support how our method works.

3 Demonstrations with injected GW signals

In this section, we discuss how ICA extracts GW using test problems. The main topic of discussion is the level at which we can apply ICA for signal extraction, that is, the applicable characteristics of the signals.

3.1 Injections of inspiral signal to Gaussian Noise

The first test is the injection of an inspiral-wave signal in Gaussian noise.

We prepared two different Gaussian-type noises, $n_{1\mathrm{G}}$ and $n_{2\mathrm{G}}$ over the flat power-spectral density, and injected h_{insp} into them as

$$\text{Model 1}: \begin{cases} x_1(t) = n_{1\mathrm{G}}(t) + h_{\mathrm{insp}}(t; t_c, M_c), \\ x_2(t) = n_{2\mathrm{G}}(t) + h_{\mathrm{insp}}(t; t_c, M_c). \end{cases} \quad (12)$$

If we apply the same Gaussian noise for both $x_1(t)$ and $x_2(t)$, then the test is the same as the well-known blind signal separation problem. Model 1, however, is somewhat challenging for weakly injected signals.

Table 1: Results of Model 1 [injection of inspiral wave to the Gaussian noise]: the signal strength $\mathcal{A}$, the fitting parameter α and β of the Fourier spectrum of the extracted signal are listed. Note that $\alpha = 15.3$ and $\beta = 0.63$ for the injected signal.

$\lvert h_{\mathrm{insp}}(t=1)\rvert$	$\mathcal{A}$	α	β	ref.
5.0	2.21	13.7	0.665	Fig.1(a4)
2.5	1.67	7.53	0.706	Fig.1(b4)
1.0	1.28	−57.5	0.661	Fig.1(c4)

We prepare one-second data with a sampling rate of 4096, and two Gaussian noises with average amplitudes of $\overline{|n_{1\mathrm{G}}|^2} = \overline{|n_{2\mathrm{G}}|^2} = 1$. For inspiral signals, we set $M_c = 26.12 M_\odot$, which is of $30M_\odot$-$30M_\odot$ binary at the observed frame, $t_c = 1.0 + 1/4096$ (*i.e.* the moment of the merger is out of the range), and compare three cases of its amplitude $|h_{\mathrm{insp}}(t=1)| = 5.0, 2.5$, and 1.0.(Note that the signals are amplified five times during one second.)

The results for the largest amplitude case are shown in Figure 1. Figure 1 (a1) shows the input signals, demonstrating that the inspiral behavior can be observed by eye at frequencies above 30 Hz. Figure 1 (a2) shows the Fourier spectrum of (a1). Figure 1 (a3) and (a4) show the ICA output results. Please note that the ICA results do not include information on the strength of each mode; in other words, the amplitude of the output data does not reflect its strength in the input data.

To see how the extracted signal matches the injected signal we approximate the power spectrum of the output signal [Figure 1(a4)] with the function $(f-\alpha)^{-\beta}$ for $f = [20, 300]$ Hz where α, β are constants, and compare them with those of the injected signal, $(f-15.3)^{-0.63}$. A comparison of the three cases is shown in Table 1. We performed the same extraction 10 times changing the initial guess of $\boldsymbol{w}_p$ randomly each time, and show the average of the fitting parameters α and β in the table. As expected, when the amplitude of the injected signals is large, the ICA clearly identifies the signal. As can be seen in Figure 1(b) and (c), identification is difficult when the amplitude of the injected signal is at the same level as the noise.

3.2 Injections of GW signal to real detector data

Next, we demonstrate the signal extraction of the injected waves from the real detector data. We used the detector data around GW150914 (GPS time of $t_c = 1126259462.4$) of LIGO-Hanford, $n_{\mathrm{H}}(t)$, and LIGO-Livingston, $n_{\mathrm{L}}(t)$, which we downloaded from GWOSC.

We made two tests. One is the injection of a sinusoidal wave,

$$\text{Model 2}: \begin{cases} x_1(t) = n_{\mathrm{H}}(t) + \sin(2\pi f t), \\ x_2(t) = n_{\mathrm{L}}(t) + \sin(2\pi f t) \end{cases} \quad (13)$$

and the other is an inspiral wave [eq.(8)],

$$\text{Model 3}: \begin{cases} s_1(t) = n_{\mathrm{H}}(t) + h_{\mathrm{insp}}(t; t_0, M_c), \\ s_2(t) = n_{\mathrm{L}}(t) + h_{\mathrm{insp}}(t; t_0, M_c). \end{cases} \quad (14)$$

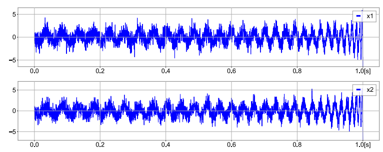

(a1) Input signals with $|h_{\text{insp}}(t=1)| = 5.0$.

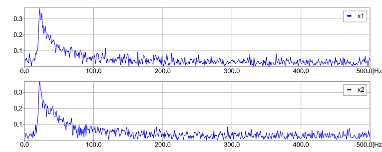

(a2) Fourier spectrum of (a1).

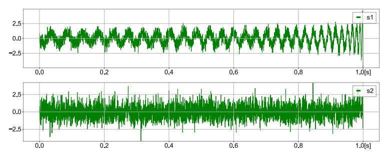

(a3) Output of ICA for (a1).

(a4) Fourier spectrum of (a3).

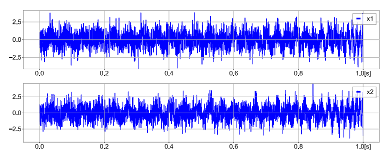

(b1) Input signals with $|h_{\text{insp}}(t=1)| = 2.5$.

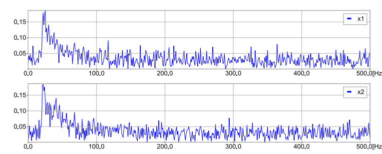

(b2) Fourier spectrum of (b1).

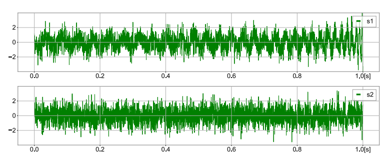

(b3) Output of ICA for (b1).

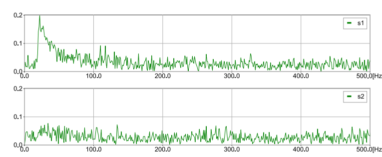

(b4) Fourier spectrum of (b3).

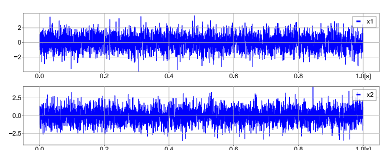

(c1) Input signals with $|h_{\text{insp}}(t=1)| = 1.0$.

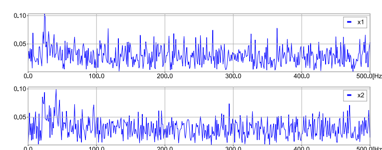

(c2) Fourier spectrum of (c1).

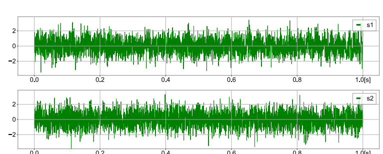

(c3) Output of ICA for (c1).

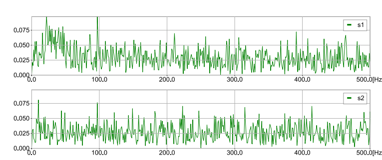

(c4) Fourier spectrum of (c3).

Figure 1: An example of GW extraction using ICA, in the case of Model 1 [eq. (12)], involving the injection of an inspiral wave into a Gaussian background. Figures are of $|h_{\text{insp}}(t=1)|/\overline{|n_{\text{G}}(t)|} = 5.0$ (a1-a4), 2.5 (b1-b4), and 1.0 (c1-c4). We use data with a length of one second, with $t = [0, 1]$, and $t_c = 1 + 1/4096$.

Table 2: Results of Model 2 [injection of sinusoidal wave to the real detector data]: SNR and excess power spectrum of 213 Hz in the extracted data over the average of 150-2050 Hz.

SNR to h_H	SNR to h_L	excess power	ref.
20.8	20.0	7.78	Fig.2(a4)
10.4	10.0	3.76	Fig.2(b4)
5.2	5.0	1.93	Fig.2(c4)

For Model 2, we used dataset of two second around the merger time of GW150914, and we set $f = 213$ Hz which is independent of the known line noises. Figure 2 and Table 2 show the results of Model 2. By changing the amplitude, we show the cases with signal-to-noise ratios (SNR) of 20 (Fig.(a)), (b)10 and (c) 5. Figures (a1), (b1), and (c1) are the input data of $x_1(t)$ and $x_2(t)$, with only the central one-second segment displayed. Figures (a2), (b2), and (c2) show the Fourier spectra of (a1), (b1), and (c1), respectively. The model uses actual detector data with different noise levels and include a variety of noise types. Therefore, if the same signal is injected into the Hanford (x1) and Livingston (x2) data, they will appear different. Figures (a3), (b3), and (c3) are the outputs of ICA, and (a4), (b4), and (c4) are their respective Fourier spectra. To judge whether the injected wave was extracted by ICA, Table 2 shows the ratio of the 213 Hz power spectrum to the average power spectrum between 150 and 250 Hz. We think the reason for the imperfect separation is the strong line noise at 60 Hz and 120 Hz in the original data. We are confident that the extraction was effective for cases with an SNR of at least 10.

For Model 3, we used one-second data before one second of merger time (t_c) of GW150914. The injected inspiral wave is $h(t; t_c - 1\text{ s}, 26M_\odot)$. The results are shown in Figure 3, using the same notation as in the previous figures. Note that we filtered over $f > 300$ Hz and that the input data had strong line noise at 60 Hz. The SNR of the injected signal is 20.9 (a1-a4), 16.8 (b1-b4), and 10.5 (c1-c4). The inspiral feature is visible in the Fourier spectrum of the output data for an SNR > 15.

4 Applications to real GW extractions

In this section, we demonstrate GW extractions of the real events.

4.1 GW150914

Here, we present a detailed analysis of the GW150914[1] event. This is the first GW detection and has been well tested as the standard. The event was observed by the Hanford (H) and Livingston (L) observatories, and the announced network-SNR in GWOSC was 26.0.

We used one-second data around t_c with a sampling rate of 4096. As a preprocessing step, we whitened the data using the power spectral density of each detector and filtered the data to [20, 300] Hz. By shifting Livingston's data every 1/4096 s, we applied ICA with five different initial weight matrices $\boldsymbol{w}_i^{(p=0)}$ and searched the dataset that showed the maximum signal strength $\mathcal{A}$ [eq. (10)]. These calculations took only 90 s on a laptop to produce the optimal $\mathcal{A}$ result.

We determined the maximum $\mathcal{A}$ when $\Delta t_{\rm HL} = -7.32$ ms. Figure 5 shows $\mathcal{A}$ as a function of $\Delta t_{\rm HL}$. The plot includes the results of our five different initial weight matrices $\boldsymbol{w}_i^{(0)}$, and we see that the values of $\mathcal{A}$ are slightly different from the initial value $\boldsymbol{w}_i^{(0)}$, but the Δt of the maximum of $\mathcal{A}$ is independent of $\boldsymbol{w}_i^{(0)}$, and is uniquely determined. From Figure 5, we estimate $\Delta t_{\rm HL}$ with an error bar of ± 0.15 ms (we used the full width at half maximum (FWHM), which corresponds to a confidence level of 76% for a normal distribution). Note that the LIGO-Virgo paper [1] denotes $\Delta t_{\rm HL} = -6.9^{+0.5}_{-0.4}$ ms with a 90% C.L. Our number is consistent with [1] and has a smaller errorbar.

We plot the input data (x1, x2) and output data (s1, s2) for the largest case of $\mathcal{A}$ in Figure 4. For the output data s1 [in Figure 4(c)], we next searched the best-matched inspiral waveform, $h_{\rm insp}(t; t_c, M_c)$, by changing M_c and the amplitude, measuring its residuals, $\mathcal{R}$. We found that $M_c = 30.8M_\odot$ produced the lowest residuals. This case is shown in Figure 6, and we can see how output s1 is similar to the expected inspiral signal.

The GWOSC webpage shows $M_c = 28.6^{+1.7}_{-1.5}M_\odot$ as an estimated value in the source frame. Our M_c is in the observed frame, which differs from the

$$M_c^{\rm obs} = M_c^{\rm source}(1 + z) \tag{15}$$

where z is the redshift parameter of the source. From the error bars in $M_c^{\rm source}$ in the GWOSC data, we calculate z (hereafter we denote $z_{\rm ICA}$) as $z_{\rm ICA} = 0.077 \pm 0.06$. The redshift z of GW150914 on the

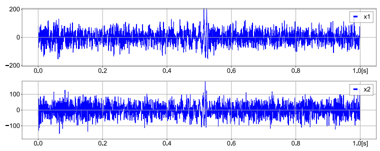

(a1) Input signals of SNR 20.

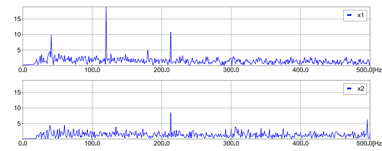

(a2) Fourier spectrum of (a1).

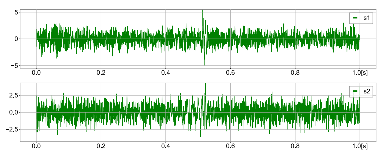

(a3) Output of ICA for (a1).

(a4) Fourier spectrum of (a3).

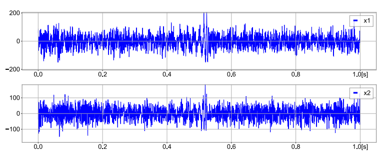

(b1) Input signals of SNR 10.

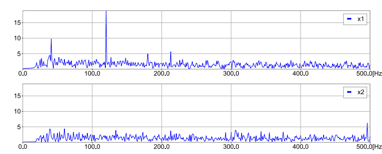

(b2) Fourier spectrum of (b1).

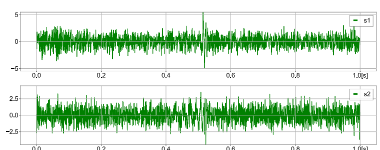

(b3) Output of ICA for (b1).

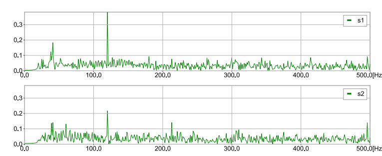

(b4) Fourier spectrum of (b3).

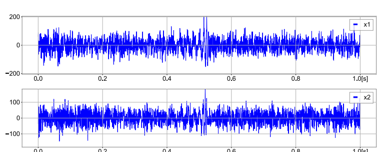

(c1) Input signals of SNR 5.

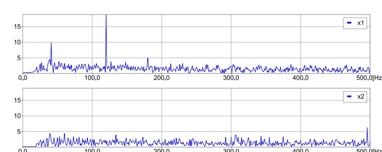

(c2) Fourier spectrum of (c1).

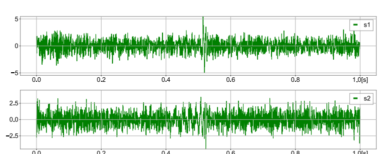

(c3) Output of ICA for (c1).

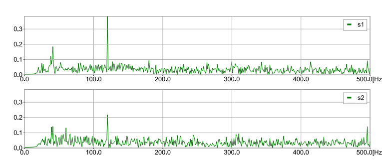

(c4) Fourier spectrum of (c3).

Figure 2: Test of GW extraction using ICA: the case of Model 2 [eq. (13)], injections of a sinusoidal wave of 213 Hz to the Hanford and Livingston data around the GW150914 event. (Note that the original data includes significant noise at 60 Hz and 120 Hz.) The signal-to-noise ratio (SNR) is 20 (a1-a4), 10 (b1-b4), and 5 (c1-c4). We see the injected wave is clearly extracted for (a) and (b), but not for (c).

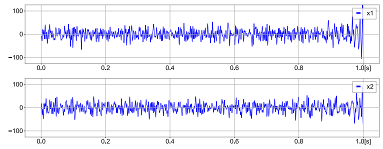

(a1) Input signals of SNR 20.9.

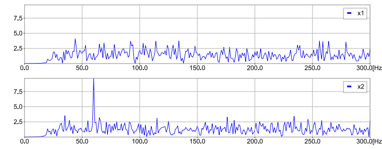

(a2) Fourier spectrum of (a1).

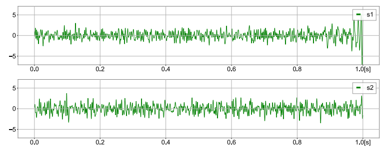

(a3) Output of ICA for (a1).

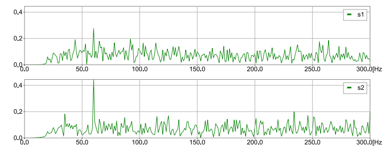

(a4) Fourier spectrum of (a3).

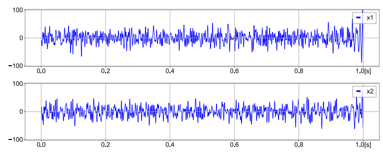

(b1) Input signals of SNR 16.8.

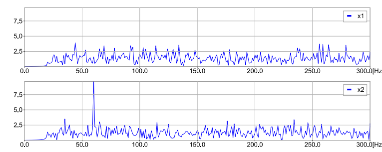

(b2) Fourier spectrum of (b1).

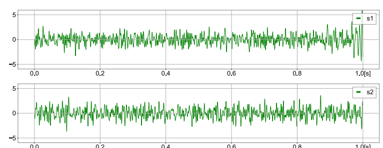

(b3) Output of ICA for (b1).

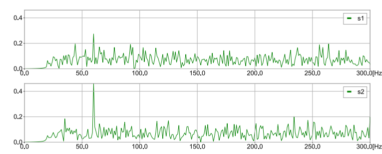

(b4) Fourier spectrum of (b3).

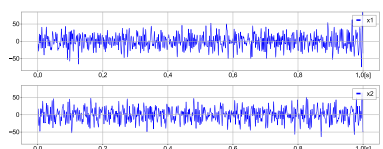

(c1) Input signals of SNR 10.5.

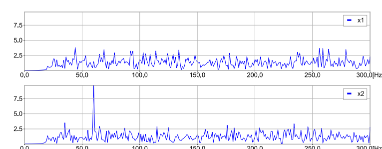

(c2) Fourier spectrum of (c1)

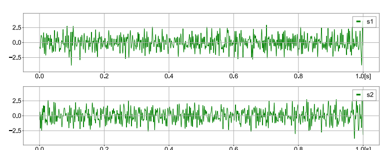

(c3) Output of ICA for (c1).

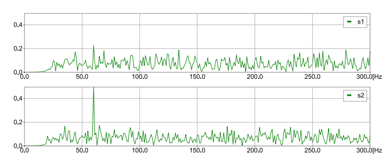

(c4) Fourier spectrum of (c3).

Figure 3: Test of GW extraction using ICA: the case of Model 3 [eq. (14)], injections of a inspiral wave signal into the Hanford and Livingston data one second before the GW150914 event. The SNR of the injected signal is 20.9 (a1-a4), 16.8 (b1-b4), and 10.5 (c1-c4). The inspiral feature is visible in the Fourier spectrum of the output data for SNR > 15. Note that we filtered for $f > 300$ Hz and also that the input data has strong line noise at 60 Hz.

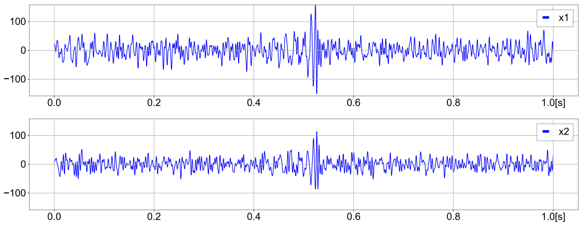

(a) Input signals with $\Delta t_{\mathrm{HL}} = -7.32$ ms. The data x1 and x2 are of Hanford and Livingston data, respectively.

(b) Fourier spectrum of (a).

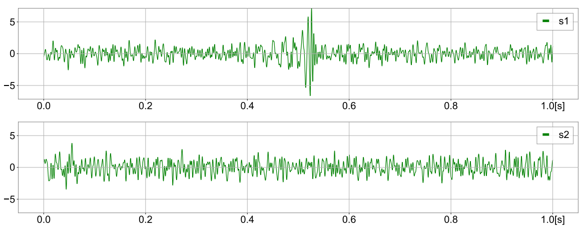

(c) ICA output.

(d) Fourier spectrum of (c).

Figure 4: Application to GW150914. (a/b) The input dataset and its spectrum with $\Delta t_{\mathrm{HL}} = -7.32$ ms which show the largest $\mathcal{A}$ in the ICA output. The x1 and x2 indicates the data of Hanford and Livingston, respectively. (c/d) The ICA output, and its spectrum. We clearly see the signal (s1) is separated from the other (s2). Note that the input data has a line noise at 120 Hz.

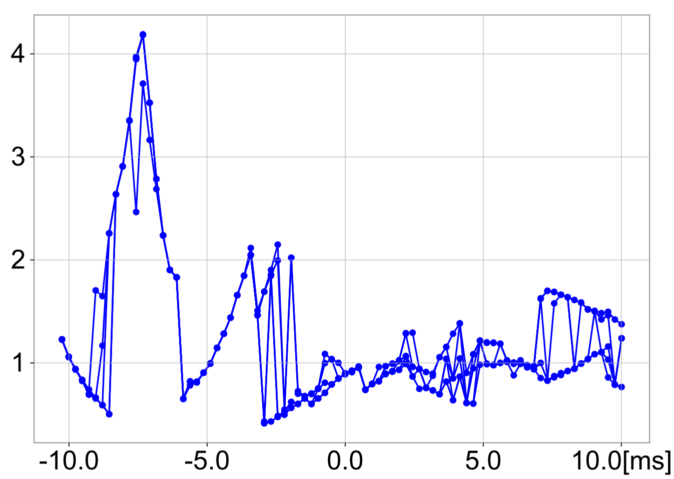

Figure 5: The strength of the extracted signal, $\mathcal{A}$ [eq. (10)] as a function of Δt_{HL} for the GW150914 case. Five trials with different initial weight matrices are plotted for each Δt_{HL}. The maximum is at $\Delta t_{\mathrm{HL}} = -7.32^{+0.15}_{-0.15}$ ms (the error is from the full width at half maximum). Note that the LIGO-Virgo paper [1] shows $\Delta t_{\mathrm{HL}} = -6.9^{+0.5}_{-0.4}$ ms.

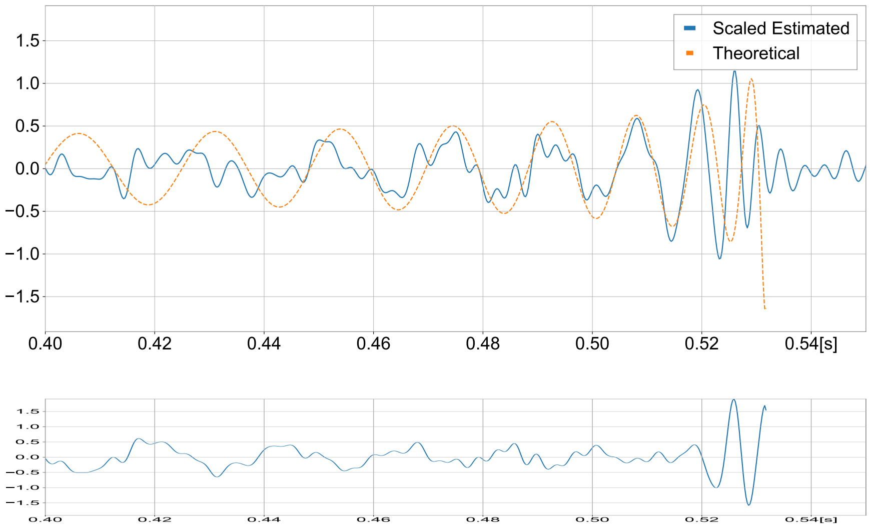

Figure 6: Extraction of GW150914. (Upper) The output data (Fig. 4 (c) s1) is overlaid with $h_{\rm insp}(t; t_c, M_c = 30.8 M_\odot)$. (Lower) The residuals.

GWOSC webpage is $z = 0.09 \pm 0.03$. Therefore our result is again consistent with theirs.

4.2 Other events

We conduct a similar analysis of other GW events from binary BHs with a higher SNR events in O1-O3. Figure 7 shows the input data (x1, x2, x3) and the output data (s1, s2, s3) that show the largest $\mathcal{A}$. For three-detector events, we performed a 2-dimensional search by shifting data, which required a maximum of 20,100 combinations, and took approximately 20 hours to compute. The ICA results are summarized in Tables 3 and 4.

Table 3 can be used to understand how ICA works. In summary, the parameter $\mathcal{A}$, which is a measure of extraction quality, remains almost constant regardless of the SNR. The residual $\mathcal{R}$, which is a measure of how well the extracted wave can be matched to the inspiral waveform, is negatively correlated with the SNR.

Table 4 can be used to understand how realistic the ICA results are . By matching with the inspiral wave, we can specify $M_c^{\rm obs}$ for each event. With $M_c^{\rm source}$ in the GWOSC table, we compare the redshift parameter $z_{\rm ICA}$ and z in the GWOSC table. As can be seen in the table 4, all the redshift parameters are consistent.

5 Summary

Independent component analysis (ICA) was applied to extract gravitational-wave signals. The most advantageous fact is that ICA approach does not require any waveform templates beforehand. The computational cost of the ICA approach is quite low.

From the injection tests, we see that the extractions are available even from real interferometer data if the signal strength (SNR) is 15 or higher. This fact came as surprise to us, since the detector data is not Gaussian. We expect that our current limitation of SNR 15 to be reduced if the detector output is cleaned up further using advanced calibrations. We then demonstrate this method for inspiral-wave extraction in binary black-hole events, focusing on 13 high-SNR binary BH events up to O3 (GWTC-3 catalogue). As shown in Table 3 the extractions were performed for all events. As shown in Table 4 the fitted waveforms (tuned with M_c and the amplitude A) show consistent parameters, M_c and z, with those reported by the LIGO-Virgo-KAGRA collaboration, GWOSC.

ICA is based on the idea that the signal is mathematically independent of others. Only the non-

Table 3: Results of the wave extractions by ICA for large SNR events in O1-O3. The 'obs' column shows which detector (Hanford/Livingston/Virgo) observed. SNR is the network signal-to-noise ratio (centred value) which is announced in GWOSC (https://gwosc.org). $\Delta t_{\rm HL}$ is the time shift between the Hanford data and Livingston data, $t_{\rm L} - t_{\rm H}$, in ms when ICA shows the best separation of the signal. $\mathcal{A}$ is the signal strength defined by eq. (10). $\mathcal{R}$ is the residuals between the extracted waveform and estimated inspiral waveform, (11), between $[t_c - 0.15\ \text{ms}, t_c]$. See table 4 for comparisons of chirp mass and redshift.

event	obs	SNR	$\Delta t_{\rm HL}$ (ms)	$\Delta t_{\rm HV}$ (ms)	$\Delta t_{\rm LV}$ (ms)	$\mathcal{A}$	$\mathcal{R}/10^{-12}$	ref.
GW150914	HL	26.0	$-7.32\pm^{1.5}_{1.5}$	–	–	4.19	5.88	Fig.4
GW190521_074359	HL	25.9	$-6.35\pm^{0.98}_{0.49}$	–	–	1.83	10.3	Fig.7(a)
GW191109_010717	HL	17.3	$3.17\pm^{0.98}_{0.73}$	–	–	3.40	18.4	Fig.7(b)
GW191204_171526	HL	17.5	$-2.44\pm^{0.49}_{0.73}$	–	–	2.07	3.27	Fig.7(c)
GW191216_213338	HV	18.6	–	$-11.0\pm^{1.5}_{0.73}$	–	3.08	2.09	Fig.7(d)
GW200112_155838	LV	19.8	–	–	$-23.2\pm^{0.49}_{0.24}$	2.43	10.5	Fig.7(e)
GW170814	HLV	17.7	$-8.06\pm^{0.49}_{0.98}$	$0.98\pm^{2.4}_{0.24}$	–	3.54	5.07	Fig.7(f)
GW190412	HLV	19.8	$-3.91\pm^{0.24}_{0.24}$	$-13.92\pm^{0.98}_{0.49}$	–	2.21	4.40	Fig.7(g)
GW190521	HLV	14.3	$2.93\pm^{0.49}_{1.2}$	$-25.15\pm^{0.49}_{1.7}$	–	2.85	31.8	Fig.7(h)
GW190814	HLV	25.3	$2.20\pm^{0.49}_{0.24}$	$21.24\pm^{0.73}_{0.24}$	–	2.00	1.65	Fig.7(i)
GW200129_065458	HLV	26.8	$3.42\pm^{0.98}_{0.24}$	$-18.31\pm^{0.24}_{0.24}$	–	3.96	11.3	Fig.7(j)
GW200224_222234	HLV	20.0	$-3.66\pm^{2.7}_{0.24}$	$-9.28\pm^{0.24}_{0.98}$	–	3.28	13.4	Fig.7(k)
GW200311_115853	HLV	17.8	$-3.66\pm^{0.73}_{1.2}$	$-27.10\pm^{2.2}_{2.2}$	–	3.17	4.34	Fig.7(l)

Table 4: Comparisons of chirp mass, $M_c^{\rm source}$, shown in GWOSC and the one obtained by ICA,$M_c^{\rm obs}$ from the best fit inspiral-wave model. The difference can be regard as redshift factor $(1 + z_{\rm ICA})$. The redshift factor in GWOSC, z, is also shown.

			GWOSC		ICA		
event	obs	SNR	$M_c^{\rm source}/M_\odot$	z	$M_c^{\rm obs}/M_\odot$	$z_{\rm ICA}$	ref.
GW150914	HL	26.0	$28.6^{+1.7}_{-1.5}$	$0.09^{+0.03}_{-0.03}$	30.8	$0.077^{+0.06}_{-0.06}$	Fig.4
GW190521_074359	HL	25.9	$32.8^{+3.2}_{-2.8}$	$0.21^{+0.10}_{-0.10}$	36.4	$0.11^{+0.10}_{-0.10}$	Fig.7(a)
GW191109_010717	HL	17.3	$47.5^{+9.6}_{-7.5}$	$0.25^{+0.18}_{-0.12}$	53.7	$0.13^{+0.22}_{-0.19}$	Fig.7(b)
GW191204_171526	HL	17.5	$8.56^{+0.41}_{-0.28}$	$0.34^{+0.25}_{-0.18}$	11.1	$0.29^{+0.04}_{-0.06}$	Fig.7(c)
GW191216_213338	HV	18.6	$8.33^{+0.22}_{-0.19}$	$0.07^{+0.02}_{-0.03}$	9.00	$0.08^{+0.03}_{-0.03}$	Fig.7(d)
GW200112_155838	LV	19.8	$27.4^{+2.6}_{-2.1}$	$0.24^{+0.07}_{-0.08}$	32.7	$0.19^{+0.10}_{-0.10}$	Fig.7(e)
GW170814	HLV	17.7	$24.1^{+1.4}_{-1.1}$	$0.12^{+0.03}_{-0.04}$	26.0	$0.08^{+0.05}_{-0.06}$	Fig.7(f)
GW190412	HLV	19.8	$13.3^{+0.5}_{-0.5}$	$0.15^{+0.04}_{-0.04}$	14.8	$0.11^{+0.04}_{-0.04}$	Fig.7(g)
GW190521	HLV	14.3	$63.3^{+19.6}_{-14.6}$	$0.56^{+0.36}_{-0.27}$	81.7	$0.29^{+0.39}_{-0.30}$	Fig.7(h)
GW190814	HLV	25.3	$6.11^{+0.06}_{-0.05}$	$0.05^{+0.01}_{-0.01}$	6.35	$0.04^{+0.01}_{-0.01}$	Fig.7(i)
GW200129_065458	HLV	26.8	$27.2^{+2.1}_{-2.3}$	$0.18^{+0.05}_{-0.07}$	30.6	$0.13^{+0.10}_{-0.08}$	Fig.7(j)
GW200224_222234	HLV	20.0	$31.1^{+3.3}_{-2.7}$	$0.32^{+0.08}_{-0.11}$	37.6	$0.21^{+0.11}_{-0.12}$	Fig.7(k)
GW200311_115853	HLV	17.8	$26.6^{+2.4}_{-2.0}$	$0.23^{+0.05}_{-0.07}$	31.0	$0.17^{+0.09}_{-0.10}$	Fig.7(l)

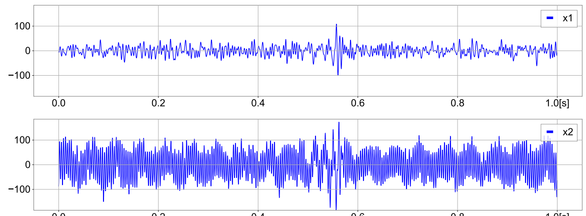

(a1) Input signals of GW190521_074359 with $\Delta t_{\rm HL} = -6.35$ ms. The data x1 and x2 are from Hanford and Livingston data, respectively.

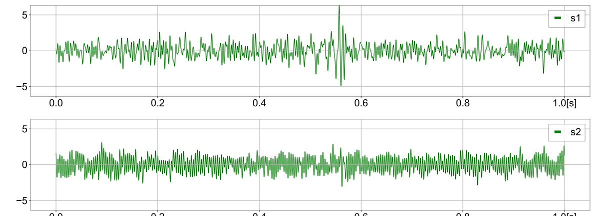

(a2) Output of ICA for GW190521_074359.

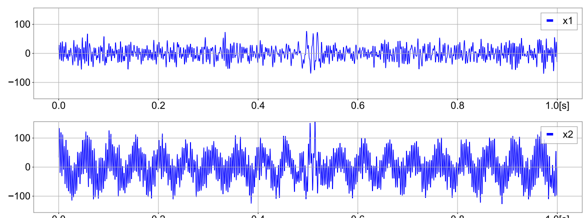

(b1) Input signals of GW191109_010717 with $\Delta t_{\rm HL} = +3.17$ ms. The data x1 and x2 are of Hanford and Livingston data, respectively.

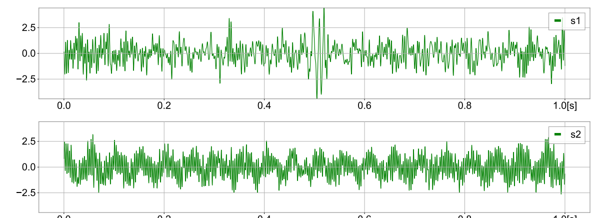

(b2) Output of ICA for GW191109_010717.

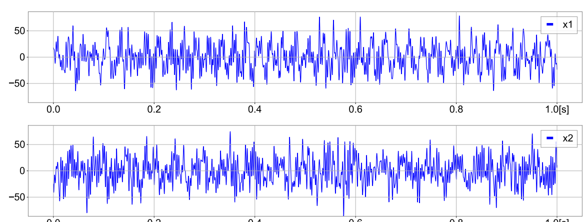

(c1) Input signals of GW191204_171526 with $\Delta t_{\rm HL} = -2.44$ ms. The data x1 and x2 are of Hanford and Livingston data, respectively.

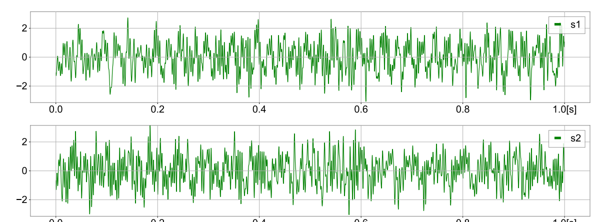

(c2) Output of ICA for GW191204_171526.

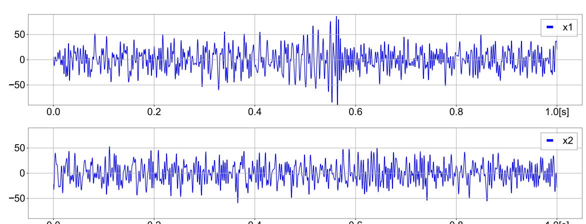

(d1) Input signals of GW191216_213338 with $\Delta t_{\rm HV} = -11.0$ ms. The data x1 and x2 are of Hanford and Virgo data, respectively.

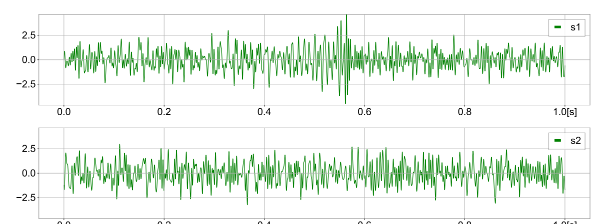

(d2) Output of ICA for GW191216_213338.

Figure 7: Input and Output data of ICA analysis.

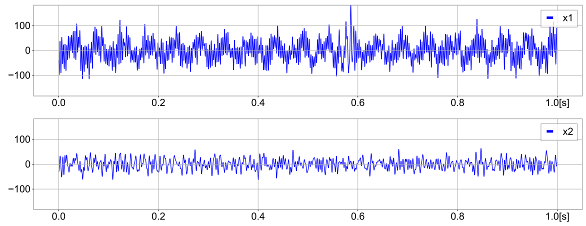

(e1) Input signals of GW200112_155838 with $\Delta t_{\mathrm{LV}} = -23.2$ ms. The data x1 and x2 are of Livingston and Virgo data, respectively.

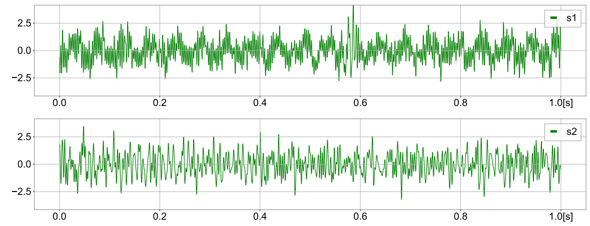

(e2) Output of ICA for GW200112_155838.

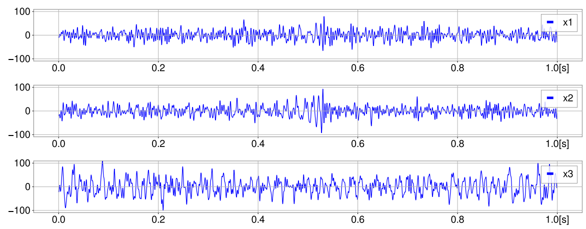

(f1) Input signals of GW170814 with $\Delta t_{\mathrm{HL}} = -8.06$ ms and $\Delta t_{\mathrm{HV}} = +0.98$ ms. The data x1, x2, and x3 are of Hanford, Livingston, and Virgo, respectively.

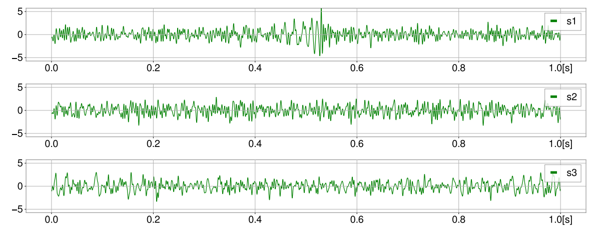

(f2) Output of ICA for GW170814.

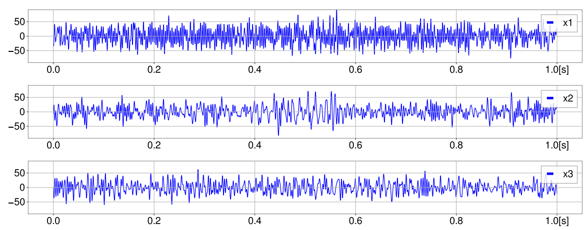

(g1) Input signals of GW190412 with $\Delta t_{\mathrm{HL}} = -3.91$ ms and $\Delta t_{\mathrm{HV}} = -13.92$ ms. The data x1, x2, and x3 are of Hanford, Livingston, and Virgo, respectively.

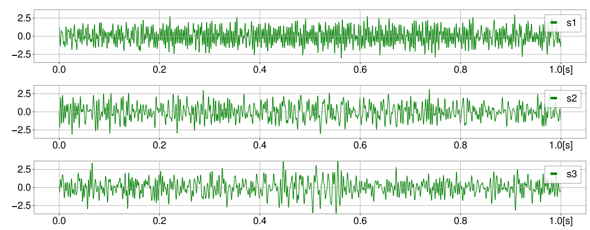

(g2) Output of ICA for GW190412.

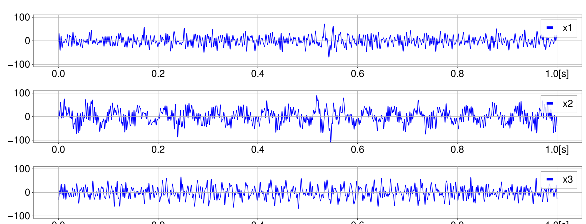

(h1) Input signals of GW190521 with $\Delta t_{\mathrm{HL}} = +2.93$ ms and $\Delta t_{\mathrm{HV}} = -25.15$ ms. The data x1, x2, and x3 are of Hanford, Livingston, and Virgo, respectively.

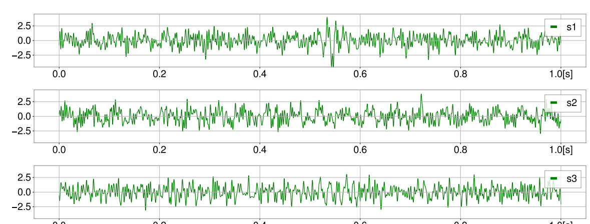

(h2) Output of ICA for GW190521.

Figure 7: Input and Output data of ICA analysis (cont.)

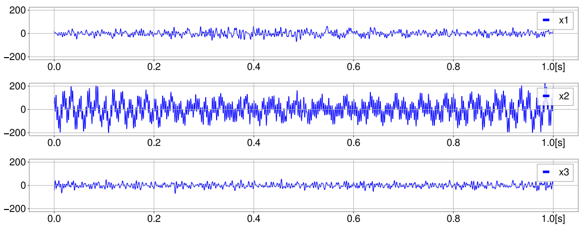

(i1) Input signals of GW190814 with $\Delta t_{\mathrm{HL}} = +2.20$ ms and $\Delta t_{\mathrm{HV}} = +21.24$ ms. The data x1, x2, and x3 are of Hanford, Livingston, and Virgo, respectively.

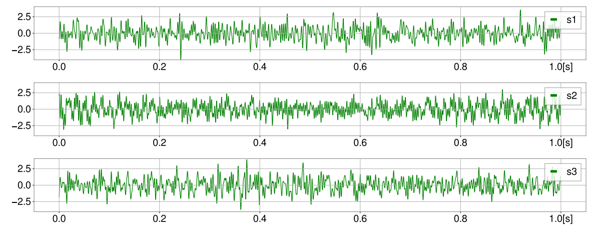

(i2) Output of ICA for GW190814.

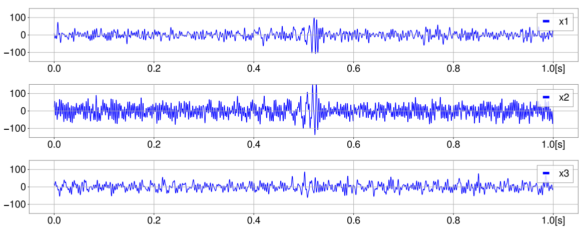

(j1) Input signals of GW200129_065458 with $\Delta t_{\mathrm{HL}} = +3.42$ ms and $\Delta t_{\mathrm{HV}} = -18.31$ ms. The data x1, x2, and x3 are of Hanford, Livingston, and Virgo, respectively.

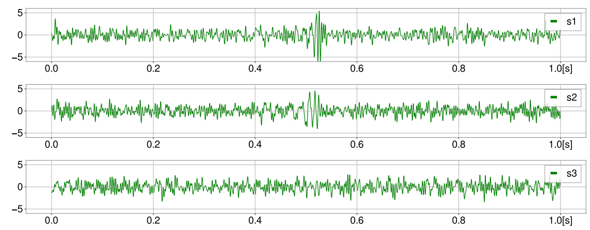

(j2) Output of ICA for GW200129_065458.

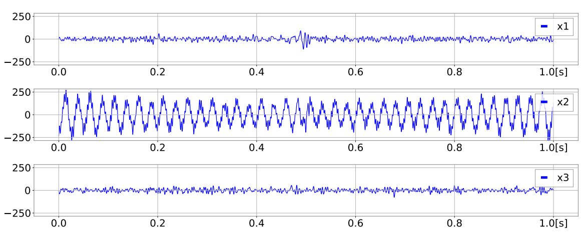

(k1) Input signals of GW200224_222234 with $\Delta t_{\mathrm{HL}} = -3.66$ ms and $\Delta t_{\mathrm{HV}} = -9.28$ ms. The data x1, x2, and x3 are of Hanford, Livingston, and Virgo, respectively.

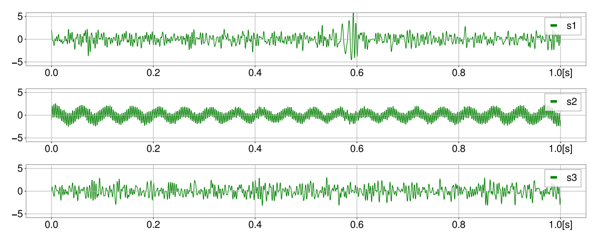

(k2) Output of ICA for GW200224_222234.

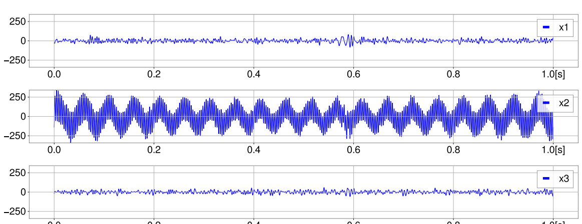

(l1) Input signals of GW200311_115853 with $\Delta t_{\mathrm{HL}} = -3.66$ ms and $\Delta t_{\mathrm{HV}} = -27.10$ ms. The data x1, x2, and x3 are of Hanford, Livingston, and Virgo, respectively.

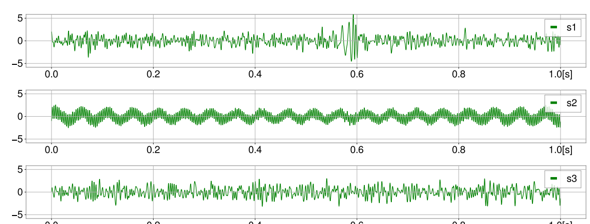

(l2) Output of ICA for GW200311_115853.

Figure 7: Input and Output data of ICA analysis (cont.)

Gaussian waves were extracted. Additionally, the current FastICA method starts by normalizing and whitening the input data, which results in output signals lacking amplitude information, and the phase can be reversed. If we have a waveform similar to those in our GWTC-3 applications, we can determine the phase by evaluating the residual, while the amplitude itself remains undetermined. The origin of the missing amplitude information comes from the initial whitening procedure. This limitation could be overcome by implementing additional procedures, e.g. applying ICA to three pairs for three-detector events and to comparing the residuals of each output data to determine a consistent amplitude parameter. Such implementations will be part of our future work.

Despite these limitations, the ICA approach is attractive because it does not use any templates in advance. Visualising the waveforms first would undoubtedly help the theoretical understanding. We believe that this approach could complement the current standard methods, particularly for testing theories of gravity and detecting unknown GW signals.

We thank Hirotaka Yuzurihara for his suggestions on the technical procedure. This work was supported by JSPS KAKENHI Grant Nos. 24K07029 and 18K03630.

A FastICA using Kurtosis

After whitening the input data $\boldsymbol{x}$ to $\boldsymbol{z}$ [Eq. (3)], one possible measure of the non-Gaussianity of the output data is to use the kurtosis of $w_i^T \boldsymbol{z}$,

$$\mathrm{kurt}(\boldsymbol{w}_i^T \boldsymbol{z}) = E[(\boldsymbol{w}_i^T \boldsymbol{z})^4] - 3\{E[(\boldsymbol{w}_i^T \boldsymbol{z})^2]\}^2. \quad (16)$$

A well-known algorithm, FastICA, detemines $\boldsymbol{w}_i$ that maximizes $\mathrm{kurt}(\boldsymbol{w}_i^T \boldsymbol{z})$. Using $E[(\boldsymbol{w}_i^T \boldsymbol{z})^2] = ||\boldsymbol{w}_i||^2$, the derivative of Eq. (16) becomes

$$\frac{\partial}{\partial \boldsymbol{w}_i} |\mathrm{kurt}(\boldsymbol{w}_i^T \boldsymbol{z})| = \begin{pmatrix} E[4(\boldsymbol{w}_i^T \boldsymbol{z})^3 \boldsymbol{z}_1] \\ E[4(\boldsymbol{w}_i^T \boldsymbol{z})^3 \boldsymbol{z}_2] \\ \vdots \end{pmatrix} - 12||\boldsymbol{w}_i||^2 \boldsymbol{w}_i. \quad (17)$$

We can, then, find $\boldsymbol{w}_i$ as in Eq. (17) can be satisfied by an iterative method, especially easily under the requirement that the norm of $\boldsymbol{w}_i$ is unity, $||\boldsymbol{w}_i||^2 = 1$. By repeating the process of finding another component $\boldsymbol{w}_i$ as each $\boldsymbol{w}_i$ satisfies its orthogonality, we can identify all possible source signals $\tilde{\boldsymbol{s}}(t)$.

However, the kurtosis method is sometimes sensitive to outliers. An alternative method is to use a mimic function to the kurtosis which we described as the "g-function" method in Eq. (5).

References

[1] B. P. Abbott *et al.* (LIGO Scientific Collaboration and Virgo Collaboration), Phys. Rev. Lett.**116**, 061102 (2016).

[2] B. P. Abbott *et al.* (LIGO Scientific Collaboration and Virgo Collaboration), Phys. Rev. Lett.**119**, 161101 (2017).

[3] R. Abbott *et al.* (LIGO Scientific Collaboration, Virgo Collaboration, and KAGRA Collaboration), Phys. Rev. X **13**, 041039 (2023).

[4] R. Abbott *et al.* (LIGO Scientific Collaboration, Virgo Collaboration, and KAGRA Collaboration) Phys. Rev. X **13**, 011048 (2023).

[5] H. Shinkai, N. Kanda, and T. Ebisuzaki, Astrophys. J.**835** 276 (2017).

[6] R. Abbott *et al.* (LIGO Scientific Collaboration, Virgo Collaboration, and KAGRA Collaboration), arXiv:2112.06861 (2021).

[7] H. Nakano, T. Narikawa, K. Oohara, K. Sakai, H. Shinkai, H. Takahashi, T. Tanaka, N. Uchikata, S. Yamamoto, & T. S. Yamamoto, Phys. Rev. D **99**, 124032 (2019).

[8] J. Veitch *et al.* Phys. Rev. D **91**, 042003 (2015).

[9] C. Messick *et al.* Phys. Rev. D **95**, 042001 (2017).
S. Sachdev *et al.* arXiv:1901.08580 (2019).
B. Ewing *et al.* Phys. Rev. D, 109, 042008 (2024).
L. Tsukada *et al.* Phys. Rev. D, 108, 043004 (2024).

[10] C. Allene *et al.* Class. Quant. Grav.**42**, 105009 (2025).

[11] A. H. Nitz, T. Dal Canton, D. Davis, & S. Reyes, Phys. Rev. D **98**, 024050 (2018).
T. Dal Canton, *et al.* Astrophys. J.**923**, 254 (2021).

[12] G. Ashton *et al.* Astrophys. J.**241**, 27 (2019).

[13] S. Hooper *et al.* Phys. Rev. D **86**, 024012 (2012).

[14] S. Klimenko, S. Mohanty, M. Rakhmanov, & G. Mitselmakher, Phys. Rev. D **72**, 122002 (2005).
S. Klimenko *et al.* Phys. Rev. D **83**, 102001

(2011).
S. Klimenko *et al.* Phys. Rev. D **93**, 042004 (2016).

[15] R. Lynch, S. Vitale, R. Essick, E. Katsavounidis, & F. Robinet, Phys. Rev. D **95**, 104046 (2017).

[16] V. Skliris, M. R. K. Norman, P. J. Sutton, arXiv:2009.14611 (2009).

[17] A. Hyvärinen, and E. Oja, Neural Networks **13** 411 (2000).

[18] A. Hyvärinen, J. Karhunen, and E. Oja, *Independent Component Analysis*, (John Wiley & Sons, 2001).

[19] A. J. Bell, T. J. Sejnowski, Neural Comput. **7**, 1129 (1995).

[20] M. Saleem, S. Datta, K. G. Arun, and B. S. Sathyaprakash, Phys. Rev. D **105**, 084062 (2022).

[21] S. Datta, M. Saleem, K. G. Arun, and B. S. Sathyaprakash, arXiv:2208.07757 (2022).

[22] R. Niu, Z-C. Ma, J-M. Chen, C. Feng, W. Zhao, Results in Phys. **57**, 107407 (2024).

[23] D. Watarai, A. Nishizawa, K. Cannon, Phys. Rev. D **109** 084058 (2024).

[24] R. De Rosa, L. A. Forte, F. Garufi, and L. Milano, Phys. Rev. D **85**, 042001 (2012).

[25] T. Akutsu *et al.* (KAGRA collaboration) Prog. Theor. Exp. Phys. **2020**, 053F01 (2020).

[26] S. Morisaki, J. Yokoyama, K. Eda, & Y. Itoh, Proc. Japan Acad. B 92, 336 [arXiv:1605.01983[gr-qc]] (2016).

[27] R. Abbott *et al.* (LIGO Scientific Collaboration, Virgo Collaboration, and KAGRA Collaboration) Astrophys. J. Suppl.**267**, 29 (2023).

[28] A. G. Abac *et al.* (LIGO Scientific Collaboration, Virgo Collaboration, and KAGRA Collaboration) arXiv:2508.18080 (2025).

[29] A. G. Abac *et al.* (LIGO Scientific Collaboration, Virgo Collaboration, and KAGRA Collaboration) arXiv:2508.18081 (2025).

[30] A. G. Abac *et al.* (LIGO Scientific Collaboration, Virgo Collaboration, and KAGRA Collaboration) arXiv:2508.18082 (2025).